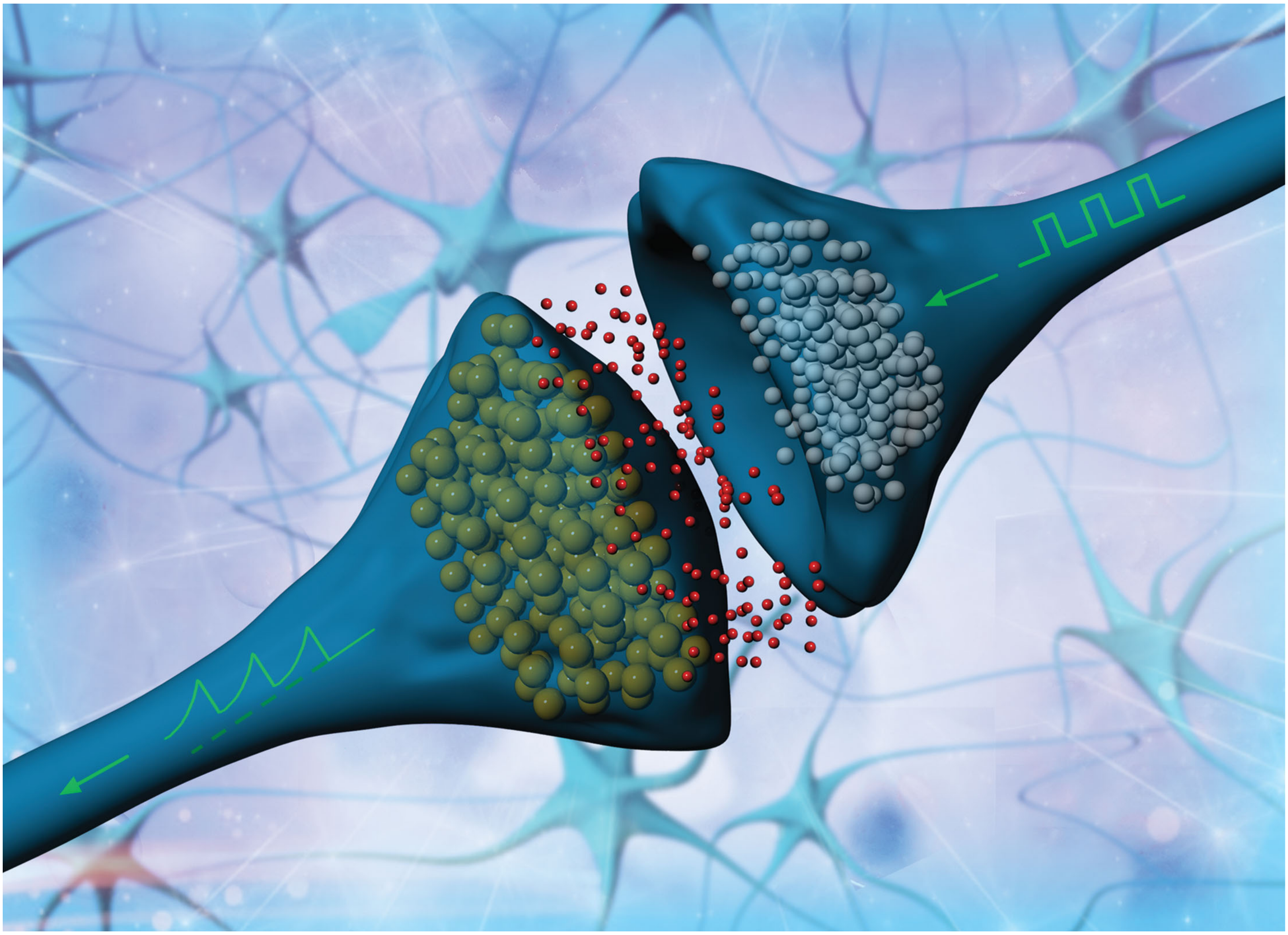

Showcasing research from the laboratory of Dr Da-Shan Shang and Prof. Young Sun at the Institute of Physics, Chinese Academy of Sciences, Beijing, China

Electrochemical-reaction-induced synaptic plasticity in MoO_x-based solid state electrochemical cells

The human brain contains ~10^{11} neurons and ~10^{15} synapses, which form a highly complex network. Information is stored and processed simultaneously through tuning the strength of the correlation between two neighboring neurons. The essential functions of biological synapses have been demonstrated in a MoO_x-based solid state electrochemical cell. The physical mechanism of the artificial synapse is attributed to the interfacial electrochemical reaction with ambient water molecules, where protons diffuse and then intercalate into the MoO_x lattice. This synaptic device shows potential applications in artificial smart-terminal networks which can communicate with the environment.

As featured in:

PCCP

STRUCTURE

ACTIVITY

ELECTROLYTE

VACUUM

See Da-Shan Shang, Young Sun *et al.*, *Phys. Chem. Chem. Phys.*, 2017, **19**, 4190.

ROYAL SOCIETY OF CHEMISTRY

rsc.li/pccp

PCCP

PAPER

View Article Online
View Journal | View Issue

Cite this: *Phys. Chem. Chem. Phys.*, 2017, **19**, 4190

Electrochemical-reaction-induced synaptic plasticity in MoO_x-based solid state electrochemical cells

Chuan-Sen Yang, Da-Shan Shang,* Yi-Sheng Chai, Li-Qin Yan, Bao-Gen Shen and Young Sun*

Received 31st August 2016,
Accepted 3rd November 2016

DOI: 10.1039/c6cp06004h

www.rsc.org/pccp

Solid state electrochemical cells with synaptic functions have important applications in building smart-terminal networks. Here, the essential synaptic functions including potentiation and depression of synaptic weight, transition from short- to long-term plasticity, spike-rate-dependent plasticity, and spike-timing-dependent plasticity behavior were successfully realized in an Ag/MoO_x/fluorine-doped tin oxide (FTO) cell with continual resistance switching. The synaptic plasticity underlying these functions was controlled by tuning the excitatory post-synaptic current (EPSC) decay, which is determined by the applied voltage pulse number, width, frequency, and intervals between the pre- and post-spikes. The physical mechanism of the artificial synapse operation is attributed to the interfacial electrochemical reaction processes of the MoO_x films with the adsorbed water, where protons generated by water decomposition under an electric field diffused into the MoO_x films and intercalated into the lattice, leading to the short- and long-term retention of cell resistance, respectively. These results indicate the possibility of achieving advanced artificial synapses with solid state electrochemical cells and will contribute to the development of smart-terminal networking systems.

1. Introduction

The development of information technology, such as the Internet of Things (IoT), provides novel opportunities to develop smart electronic devices as terminals in every aspect of life, which can feel, memorize, think, communicate, and change next-step behavior in real time. Conventional electronic devices are becoming inefficient in this respect since their parameters and dataset are usually pre-defined, that is, set by offline training. Recently studied synaptic devices that mimic the ability of the human brain could be considered as intelligent and high-efficiency online training devices.[1] It has been known that, the human brain contains $\sim 10^{11}$ neurons, each connecting to $\sim 10^4$ other ones on average through synapses which amount to an extremely large number of 10^{15} in the human brain.[2] The information is stored and processed simultaneously through tuning synaptic weight, which is defined as the strength of correlation between two neighboring neurons, and the operation is collective and adaptive.[3–5] The particular features of the synapse, called "synaptic plasticity" in neuroscience, provide an optimal way to realize smart-terminals through building artificial synaptic devices.

Solid state electrochemical (SSE) cells with redox-based resistive switching properties currently attract much attention due to their possible application in nonvolatile memory devices.[6–8] Based on the predominant physical mechanisms, the SSE cells can be classified into two categories, that is, electrochemical metallization memory (ECM) in electrolytes or nanogaps (*e.g.* Ag_2S,[9] Cu_2S,[10] Ag-α-Si,[11] Cu–SiO_2,[12] Cu–GeSe[13]) and valence change memory (VCM) in transition metal oxides (*e.g.* $SrTiO_3$,[14] TiO_2,[15] TaO_x,[16] WO_3[17]). From the physical chemistry point of view, the mechanism of synaptic weight change is closely related with the migration of ions (such as Na^+, Ca^{2+}, K^+) between neurons.[1,4] This process is similar to the redox-based resistive switching behavior and the synaptic behaviors have been realized in both types of SSE cells recently.[18–23] However, the SSE cells, especially for ECM-type, usually show abrupt characteristics, *i.e.* digital switching, due to the high conductivity of metallic filaments formed and broken during resistance switching,[9–15] which leads to some limitations to emulate the synaptic behavior, such as implementing adaptive learning efficiency and capacity of synapse.[24] Therefore, to build an artificial synapse, SSE cells with continual resistance change, *i.e.* analog switching, are preferable and have attracted increasing attention.[24–27]

Recently, we have reported a transition from ECM-type switching into VCM-type switching in a two-terminal SSE cell with a sandwich structure of Ag/MoO_x/fluorine-doped tin oxide (FTO).[28]

Beijing National Laboratory for Condensed Matter Physics, Institute of Physics, Chinese Academy of Sciences, Beijing 100190, P. R. China.
E-mail: shangdashan@iphy.ac.cn, youngsun@iphy.ac.cn

Such a kind of transition leads to a continual change in the cell resistance and is of significance in realizing synaptic plasticity. In the present study, we systematically investigated dynamic resistance switching and its relaxation behaviors to explore their possibility of application in synaptic devices. Synaptic behaviors, such as synaptic potentiation/depression, short-term to long-term plasticity transition, spiking-rate-dependent plasticity (SRDP), and spiking-time-dependent plasticity (STDP) were successfully emulated in the SSE cell. The underlying synaptic operation mechanism was discussed based on proton diffusion and intercalation in the MoO_x films. These results help to pave the way for building artificial synaptic devices through electrochemical-reaction-induced resistance change in SSE cells. The synaptic device shows a potential application in smart-terminals which can 'communicate' with the ambient atmosphere.

2. Experimental details

Polycrystalline molybdenum oxide (MoO_x) films were deposited on a commercial glass substrate with ~100 nm thick FTO thin films through a chemical vapor deposition technique. MoO_2 and MoO_3 were used as sources in oxygen gas with a flowing rate of 60 sccm. The source and substrate temperatures were maintained at 650 and 300 °C, respectively. The pressure was kept at 120 Pa during the deposition. The film thickness is ~500 nm to reduce leakage current of the cell. The X-ray diffraction (XRD) (Rigaku Miniflex with copper K_α) and scanning electron microscopy (SEM) (HITACHI S-4800) characterization show that the as-prepared films have an orthorhombic structure and uniform grains with sizes of 120–150 nm.[28] Energy dispersive spectroscopy (EDS) (HORIBA 593-H) in ten selected areas shows that the films are composed of Mo and O with an average ratio of ~1 : 2.8 *i.e.* $MoO_{2.8}$. The top electrodes of 0.25 mm diameter were in contact with the surface of MoO_x films using silver paste and a metal mask to form a simple two-terminal cell with the bottom FTO electrode. The silver paste electrode is made of many small silver particles and forms a porous structure, which is helpful for moisture adsorption of the cell. The electric properties of the cells were measured using a Keithley SourceMeter 2611 and an Agilent Function/Arbitrary Waveform Generator 33250A. A schematic illustration of a synapse, the cell structure and measurement setup are shown in the inset of Fig. 1(b). During the measurement, a voltage was applied to the top electrode with the bottom electrode being grounded. The as-prepared cells were stressed by voltage sweep of at least ten cycles between ±5 V at a constant sweep rate of 0.25 V s^{-1} to obtain a stable state before the electrical measurement. All the electrical measurements were performed with an ambient relative humidity of ~45%.

3. Results and discussion

3.1 Resistance switching in $Ag/MoO_x/FTO$ cells

Fig. 1(b) shows typical current–voltage (I–V) curves of the cells at a constant voltage sweep rate of 0.25 V s^{-1} and a maximum bias of ±5 V. An obvious I–V hysteresis appeared. During positive sweeping, the cell conductivity decreased when the sweep voltage exceeded ~1.5 V and then the cell resistance switched to a higher resistance state (HRS). This process is defined as the

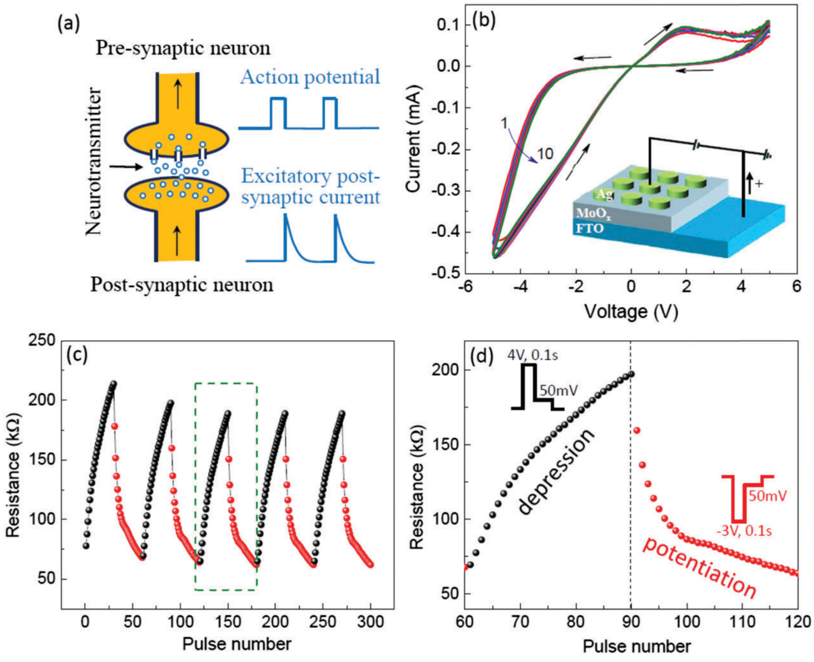

Fig. 1 (a) Schematic illustration of the biological synapse. In a synapse, the arrival of an action potential releases neurotransmitters that assist ion channels for signal transmission. (b) I–V characteristics of the cell under a voltage sweeping range of ±5 V with 10 cycles. The voltage sweep rate was 0.25 V s^{-1}. The inset shows the cell structure. (c) Gradual resistance change cycles of the cell under repeated positive (black ball, 4 V for 0.1 s spaced 1 s apart) and negative (red ball, −3 V for 0.1 s spaced 1 s apart) voltage pulses. The resistance was measured at 0.05 V. (d) Enlargement of one of the cycles in the inset of (c). The resistance increase (decrease) indicates the biological synaptic depression (potentiation).

SET process. By sweeping to negative voltages the conductivity increased when the sweep voltage was larger than ∼2.5 V and the cell resistance was RESET to the low resistance state (LRS). No abrupt change in current can be observed during the voltage sweep. Besides voltage sweeping, the cell resistance can also be adjusted gradually by only applying identical voltage pulse numbers. As shown is Fig. 1(c) and (d), 30 voltage pulses with 4 V amplitude, 0.1 s width, and 1 s space for each pulse were applied firstly to the cell. The cell resistance was measured immediately after each pulse by a reading voltage of 0.05 V. It can be seen that the cell resistance increased gradually with increasing pulse number, and then the cell resistance decreased by applying 30 identical voltage pulses with −3 V amplitude and 0.1 s width.

The resistance switching behavior is analogous to the transmission characteristics of biological synapses. A synapse is a conjunction of two neuron cells, named pre-neuron and post-neuron, as shown in Fig. 1(a). This structure is analogous to the sandwich configuration of the Ag/MoO_x/FTO cells. Under an external stimulus, spikes or action potentials from the pre-neuron can be transmitted through the synapse to the post-neuron and generate an excitatory post-synaptic current (EPSC), whose amplitudes or intensity are determined by the connection strength, *i.e.*, the synaptic weight. Here, the cell resistance can be considered as the synaptic weight, which can be tuned by an external electric field. The resistance increase and decrease signify the depression and potentiation of the synaptic weight, respectively, as it exhibits synaptic plasticity, that is, the change can last for a certain period of time. Moreover, from the viewpoint of the synaptic device, the continual resistance change by varying identical pulse numbers shows an obvious advantage over that obtained by varying pulse amplitude or width, because it could greatly simplify the design of the programming pulse generation modules.[24]

3.2 Transition from short-term to long-term plasticity

A prominent characteristic of synaptic plasticity is the presence of short-term plasticity (STP) and long-term plasticity (LTP) separated by the retention times of the synaptic weight.[29,30] Additionally, STP can be converted to LTP after sufficient training, as it provides a very practical application in allocating limited sources for the most efficient use during working. These characteristics can be realized through the short- and long-term memory effects of the cell resistance. The time scale of the memory properties can be probed by monitoring the relaxation of the cell current, that is, EPSC, after stimulation by voltage pulses.

As shown in Fig. 2(a), five voltage pulses (or spikes) with different pulse widths were applied to the same cell starting from the same initial state, and the current relaxation was recorded by

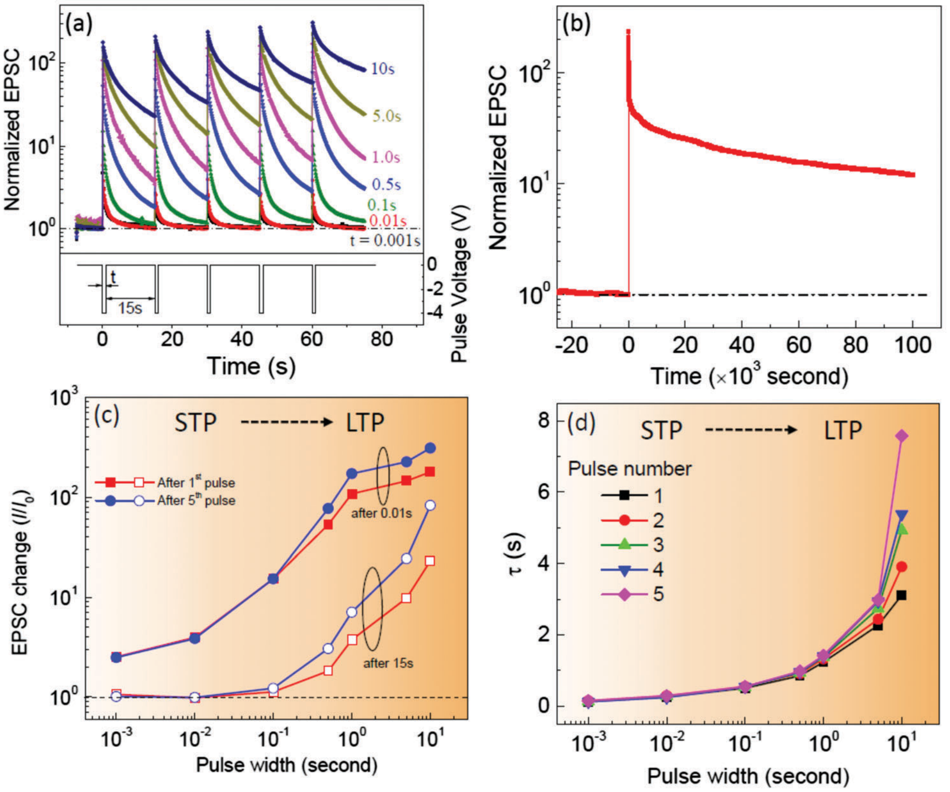

Fig. 2 (a) (Top) The formation and decay of the EPSC under a sequence of pulses containing 5 pulses with amplitude −4 V and different widths from 0.001 to 10 s and an interval of 15 s. (Bottom) Schematic illustration of the applied pulse sequence. (b) EPSC stimulated by applying 100 pulses with amplitude −4 V, a width of 0.1 s, and an interval of 0.1 s (*i.e.* frequency 10 Hz). It shows a long-term memory effect of the plasticity. (c) Dependence of the EPSC change on the pulse width. I_0 and I are the cell initial current and the current measured after the pulse stimulation, respectively. (d) The change in the relaxation time constant (τ) determined by fitting the above EPSC decay with eqn (1) with pulse width and pulse number. The gradual increase of the EPSC change ratio as well as the relaxation time constant indicate qualitatively a trend of the STP-to-LTP transition of biological synapses.

a reading voltage of 0.05 V after each pulse in the pulse series. To ensure the comparability of the conductance change with different pulse numbers and widths, 15 s was selected as the recording time. Upon the application of each pulse, the EPSC increased first, followed by a decay towards the initial value. When the pulse width is larger than 0.1 s, an overall increase of the EPSC appears despite the current decay. This can be explained by the idle time between the applied pulses not being long enough for the cell current to relax to its initial state. Therefore, the EPSC induced by application of the following voltage pulses overlapped with the residual current and then stimulated a more effective potentiation. Fig. 2(b) shows an EPSC stimulated by 100 pulses with an amplitude of −4 V, a width of 0.1 s, and an interval of 0.1 s. The EPSC cannot decay to the initial value even after 10^5 s, indicating an enhancement of the memory effect of the plasticity.

This effect can be better illustrated by calculating the EPSC change by comparing the cell current (I) measured immediately ($\sim$0.01 s) and 15 s after the pulse stimulation with the initial current (I_0). The EPSC enhancement (or synaptic potentiation) measured instantly after the pulse stimulation shows an obvious increasing dependence on the pulse width (see the red solid symbols in Fig. 2c). However, the EPSC potentiation decayed largely after 15 s. The EPSC induced by pulses with width no more than 0.1 s almost returned to its initial value, which could be defined as a STP behavior. With increasing pulse width, a part of EPSC potentiation remained after 15 s, implying a trend of transition from STP to LTP behavior. The EPSC measured after the 5th pulse shows the same dependence on the pulse width. However, a larger EPSC potentiation was observed in the long-term regime, which resulted from the cumulative effect of overlapping with increasing pulse numbers. The EPSC can be well fitted by a stretched-exponential function[21]

$$I(t) = I_0 \exp\left[-\left(\frac{t}{\tau}\right)^{\beta}\right] \tag{1}$$

where I_0 is the pre-factor, t is the time, τ is the characteristic relaxation time constant, and β is the stretching index ranging between 0 and 1. The synaptic memory ability and synaptic weight can be represented by τ and I_0, respectively.[31] As shown in Fig. 2(d), τ was gradually enlarged by almost 70-fold upon increasing the pulse width as well as the pulse number. The increasing value of τ indicates that the current takes much longer to decay. Similar phenomena have also been observed in other resistive switching devices and were considered as a clear indication of the STP-to-LTP transition.[19,21] It should be pointed out that the STP and LTP are just comparative terms, since there is no unified criterion of timescale to judge the short- and long-term memory. From the viewpoint of device application, it depends on the real service conditions of the memory or sensor devices.

3.3 Implementation of spike-rate-dependent plasticity

Besides the pulse width and pulse number, the length of the idle time between the applied pulses, that is, the applied pulse frequency, can also have a significant effect on the synaptic properties of the SSE cells. It is natural to expect that the shorter the pulse interval is, the stronger the EPSC value becomes and remains. Biologically, the pulse frequency effect on the synaptic plasticity is manifested as the spike-rate-dependent plasticity (SRDP),[32] which is a widely observed synaptic learning rule across different kinds of synapses.[33,34] To demonstrate the pulse frequency effect, we applied a sequence of pulses with different frequencies to our cells and then examined the residual EPSC potentiation. Fig. 3 shows the EPSC measured 15 s after applying 10 consecutive pulses, in which the pulse widths were 0.01 and 0.1 s, the pulse voltage was fixed at −4 V, and the pulse frequency changed from 0.1 to 100 Hz. Upon increasing the pulse frequency, the residual EPSC potentiation was detected by calculating the change ratio (I/I_0), where I is the first measured data point value and I_0 is the initial current under the reading voltage 0.05 V. As shown in Fig. 3(d), I/I_0 increased even though the pulse width was 0.01 s. When increasing the pulse width to 0.1 s, the residual EPSC potentiation enhanced more significantly, which is in accordance with the results in Fig. 2(c). On the other hand, it can be seen that the EPSC decay occurred slowly (see Fig. 3c), indicating a longer memory effect of the plasticity with the increasing pulse frequency. This property indicates that the synaptic function of STP-to-LTP transition could also be emulated through the change in the applied pulse frequency.

3.4 Implementation of spike-timing-dependent plasticity

Spike-timing-dependent plasticity (STDP) is an important synaptic learning rule that defines how a synapse participates in information processing and brain network functions.[35,36] In this rule, synaptic plasticity or synaptic weight depends on the temporal correlation between pre- and post-synaptic spikes. If the pre-synaptic spike precedes (lags) post-synaptic spike repeatedly, the synapse weight potentiates (depresses), *i.e.* the synaptic weight or conductance increases (decreases).[19] Previously, both the pre- and post-synaptic spikes were formed by a pulse protocol containing both positive and negative pulses, and the STDP was realized by changing the overlapping time between the pre- and post-pulse protocols.[19,23,37] In the current cells, however, it has been demonstrated that the applied pulse width and frequency have strong effects on the EPSC-spike interactions. Therefore, it is possible to realize the STDP property simply through the modulation of pre- and post-synaptic spike intervals, which determine the overlapping between EPSC stimulated by the former spike and the subsequent spike. This method has been understood recently as a second-order memristor model.[38]

In our cells, the top and bottom electrodes play the role of the pre- and post-synaptic neurons, respectively, and the spike is simulated by applying voltage pulses with different polarities. Similar to Ca^{2+}-concentration dependent synaptic weight change in biological synapses,[39] the natural diffusion of accumulated protons and subdued electrochemical reactions give rise to the decay (fitted by SEF) of the synaptic weight after the pre-synaptic spike was applied in our cells. If a post-synaptic spike is applied within the relaxation time of the pre-synaptic one, the synaptic weight will be the collective effect of both spikes and can be strongly influenced by the time the last spike was applied,

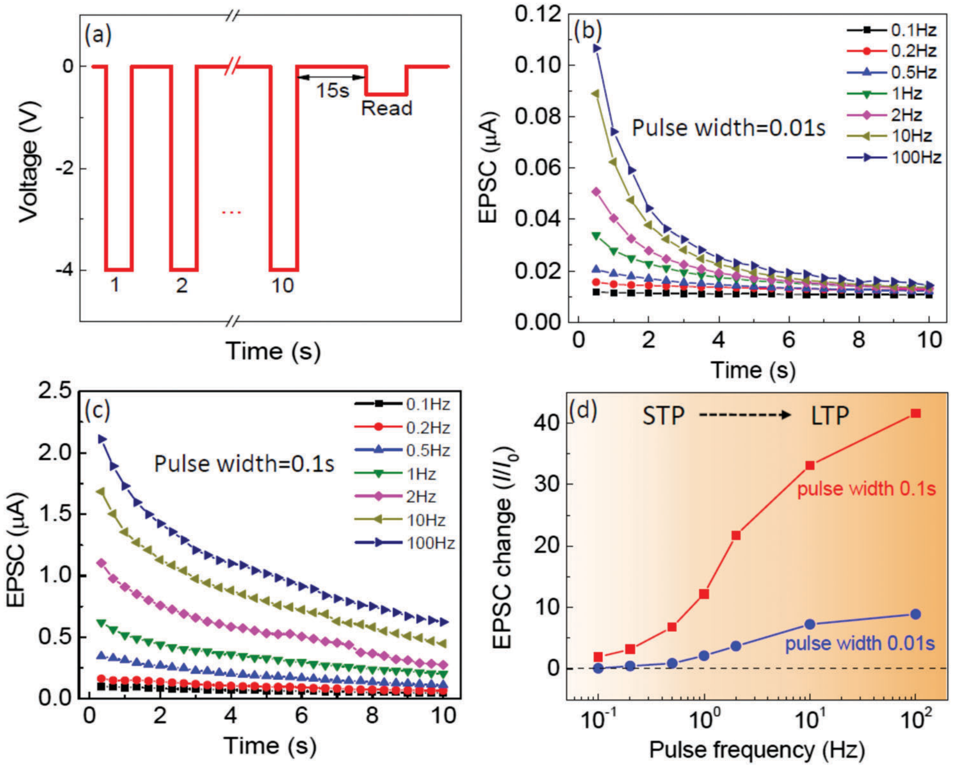

Fig. 3 (a) The schematic illustration of the applied pulse sequences. The EPSC was measured 15 s after applying 10 consecutive pulses and for 10 s. The pulse amplitude and reading voltage were fixed at −4 V and 0.05 V, respectively. The pulse widths were (b) 0.01 s and (c) 0.1 s. (d) Dependence of the EPSC change ratio on the frequency of the applied pulse sequence. The EPSC change ratio was calculated by comparing the first measured data point value (I) in (a) and (b) at each frequency with the initial current (I_0) under the reading voltage 0.05 V. The gradual increase of the EPSC change ratio indicates qualitatively a trend of the STP-to-LTP transition of biological synapses.

that is, the time interval of the two spikes. To implement STDP with the current cells, a series of pulses containing two negative voltage pulses (−4 V, 0.1 s) representing the pre-synaptic spike and two positive voltage pulses (5 V, 0.1 s) representing the post-synaptic spike were exerted on the cells and the EPSC change was measured. Selecting two pulses as one pre- or post-synaptic spike is for the enhancement of the EPSC signal and then the enhancement of the interaction between the pre- and post-synaptic spikes. The relative timing Δt is defined as the interval between the end of the pre-synaptic spike and the beginning of the post-synaptic spike, as schematically shown in Fig. 4(a). To evaluate the relaxation of the STDP behavior in the cells, the EPSC amplitude was measured at a series of read delay times (t_m = 0.1, 1.0, 5.0, 10.0 s) after the last pulse and compared to

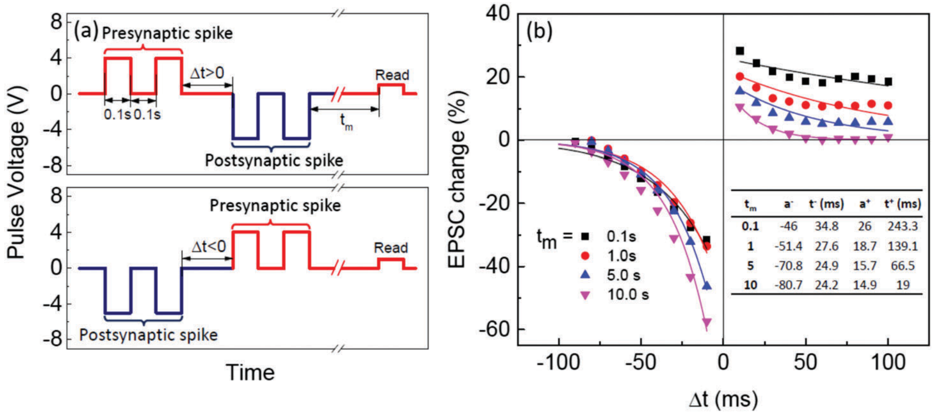

t_m	a^-	t^- (ms)	a^+	t^+ (ms)
0.1	-46	34.8	26	243.3
1	-51.4	27.6	18.7	139.1
5	-70.8	24.9	15.7	66.5
10	-80.7	24.2	14.9	19

Fig. 4 (a) Schematic illustration of a pair of pre- and post-synaptic spikes, which are designed to implement STDP function. For the enhancement of the EPSC signal, two negative voltage pulses (−4 V, 0.1 s) and two positive voltage pulses (5 V, 0.1 s) were used to represent one pre- and post-synaptic spike. (b) The relative change of the EPSC change, *i.e.* synaptic weight (ΔW) *versus* the relative spiking time (Δt). The solid lines are the exponential fits by eqn (2) to the experimental data. Inset: The obtained fitting parameters.

that of the reference value, which was measured prior to the pulse application. Then, the cell was relaxed to the initial state with an error value lower than 5 percent. For saving time, several voltage pulses with ±3 V amplitude and 0.1 s width were used to accelerate the restoration. The experiment was repeated for different Δt. The effect analogous to the STDP learning function was implemented in our SSE cells by applying the non-overlapping pre- and post-synaptic spike protocol. As shown in Fig. 4(b), the cell resistance increased (decreased) when $\Delta t > 0$ ($\Delta t < 0$), meaning that the current change direction depends on the latter two pulses. This observation can be attributed to the intrinsic decay trend of the EPSC, which is always opposite to the polarity of the applied pre-synaptic (or post-synaptic) spike but identical to the polarity of the subsequent post-synaptic (or pre-synaptic) spike, resulting in a more effective potentiation of the latter spike.

Moreover, the EPSC change ratio is determined by the time interval Δt. The longer Δt, the lower the absolute value of ΔW. This behavior can be attributed to the decrease of the residual current with increasing Δt. The EPSC change (ΔW) *versus* Δt can be well fitted by the STDP learning functions[23,40]

$$\Delta W(\Delta t) = \begin{cases} a^{+}\exp(-\Delta t/\tau^{+}) & \text{if } \Delta t > 0 \\ -a^{-}\exp(\Delta t/\tau^{-}) & \text{if } \Delta t < 0 \end{cases} \tag{2}$$

where a^{+}/a^{-} is the scaling factor and τ^{+}/τ^{-} is the time constant for $\Delta t > 0/\Delta t < 0$, respectively. The fitting parameters are shown in the inset of Fig. 4(b). The a^{+}/a^{-} and τ^{+}/τ^{-} values are comparable with those values observed in biological synapses.[3,41] The EPSC change is also influenced by the read delay time t_m. The increase of t_m results in the increase (decrease) of τ^{+}/τ^{-} when $\Delta t > 0$ ($\Delta t < 0$). This property provides a way to tune the time constant of the STDP function by changing the read delay time, which is critical to the application of electronic synapses for different computation tasks in neuromorphic functions.

3.5 Discussion of the mechanism of synaptic plasticity

Two main mechanisms, that is, ECM and VCM, for the resistance switching in SSE cells have been reported, and mainly concern the formation and rupture/re-formation of conductive filaments.[6] In our cells, the possibility of the ECM switching has been excluded due to the switching polarity as well as the continual resistance change,[28] although a silver electrode was used. It has been demonstrated that the *I*–*V* hysteresis was humidity dependent and no resistance switching was observed under vacuum and dry oxygen conditions.[28] Fig. 5(a) shows the construction of a MoO_x-based SSE cell with an Ag electrode and a counter FTO electrode. When a positive voltage was applied to the Ag electrode,

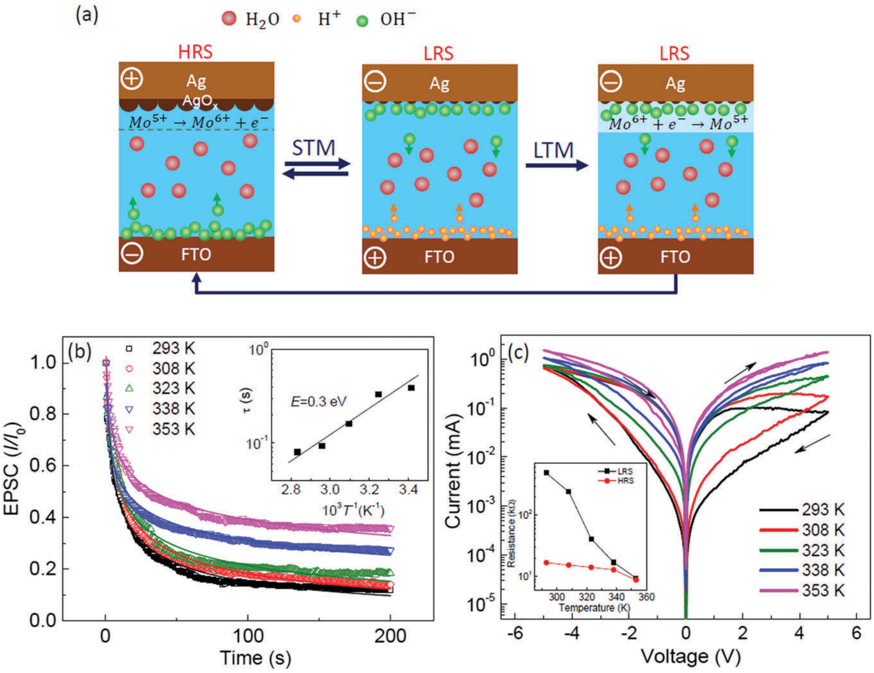

Fig. 5 (a) Schematic illustration of electrochemical processes during the voltage sweep. (Left) Upon application of a positive bias to the Ag electrode, an AgO_x layer was formed at the Ag/MoO_x interface due to anodic passivation, resulting in the oxidation of Mo^{5+} to Mo^{6+} in conjunction with the hydroxyl group generation at the counter electrode. (Middle) Upon application of a negative bias to the Ag electrode, hydroxyl groups (OH^-) and protons (H^+) were generated in the cathode and anode, respectively. The diffusion of protons as well as hydroxyl groups lead to the decay of the EPSC values with time, that is, STP behavior. (Right) Electrochemical doping process (eqn (7)) occurring near to the cathode upon increasing the pulse frequency or width, resulting in the STP-to-LTP transition. (b) The EPSC decay at different temperatures (symbols) and their fitting curve (solid line) by eqn (1). I_0 and I are the cell initial current and the current measured after the pulse stimulation, respectively. The inset shows the plot of the relaxation time constant (τ) determined by fitting the above EPSC decay *versus* the reciprocal of temperature. A line fitting gives the activation energy for diffusion E = 0.3 eV. (c) *I*–*V* characteristics of the cell under different temperatures. The sweeping speed was fixed at 0.25 V s^{-1}. The inset shows the cell resistance extracted from the *I*–*V* curves under 0.1 V, in HRS and LRS. It can be seen clearly that the *I*–*V* hysteresis, *i.e.* resistance switching, was clearly suppressed at high temperatures.

the Ag electrode was oxidized to Ag^+ ions and then reacted with hydroxyl groups (OH^-) generated by water adsorption to form an AgO_x layer at the Ag/MoO_x interface by[28]

$$Ag^+ + 2xOH^- \rightarrow AgO_x + xH_2O \tag{3}$$

This procedure is defined as anodic passivation, which impeded further oxidation of the Ag electrode as well as Ag^+ migration into the films. Because Ag^+ ions do not pre-exist in the MoO_x film, a counter electrode reaction is required for providing the counter charge.[28,42,43] Water molecules adsorbed onto the film supply the counter charge according to the half-cell reaction[28,42,43]

$$H_2O + e^- \rightarrow OH^- + 1/2H_2 \tag{4}$$

$$1/2O_2 + H_2O + 2e^- \rightarrow 2OH^- \tag{5}$$

Correspondingly, the half-cell reaction of water oxidation is also plausible[28,42,43]

$$H_2O \rightarrow 1/2O_2 + 2H^+ + 2e^- \tag{6}$$

After anodic passivation, the electrochemical reaction proceeded with water reduction at the cathode in conjunction with oxidation of Mo^{5+} ions, if there were some, near the anode, resulting in a more insulating state of the film. Therefore, the SSE cell switched to the HRS, which corresponds to the synaptic depression process. Note that the cell resistance shows a more significant change in the first 50 pulse numbers (see Fig. 1c). It might be due to some electrochemically unbalanced process among the silver electrode, MoO_x thin film, and the ambient moisture at the beginning of the voltage pulse applied.

When applying negative voltage to the Ag electrode, the decrease of the SSE cell resistance, which corresponds to the synaptic potentiation process, experienced two principal steps. Firstly, the AgO_x layer dissolved in conjunction with the excessive proton (H^+) and OH^- generation at the anode and cathode, respectively. The generated protons further improved the conductivity of the MoO_x film *via* the "Grotthuss mechanism" providing an additional protonic conductivity contribution.[44–46] Removing the voltage on this occasion, however, the protons accumulated at the interface diffused gradually due to the concentration gradient and then recombined with hydroxyl groups, resulting in the decay of the obtained LRS. The decay of LRS is analogous to the decay of the EPSC of a biological neuron, corresponding to the STP behavior. When the next spike of voltage pulse was applied with a small interval (*i.e.* high frequency), protons generated by the first spike still partially resided near the interface. Thus, the EPSC induced by the following spikes were enhanced (see Fig. 3d). Extending the spiking time (*i.e.* pulse width) achieved similar effects (see Fig. 2c and d). In the second step, upon increasing the spike frequency or time, the Mo^{6+} ions near the cathode were reduced into Mo^{5+} by proton uptake (or intercalation) and accepting electrons from the cathode, which could be described by

$$Mo^{6+}O_3 + e^- + H^+ \rightarrow Mo^{5+}(O_2)(OH) \tag{7}$$

This reaction can be seen as an electrochemical doping process, in which the weakly-adsorbed protons were intercalated into the lattice and gave rise to an energetically stable phase, such as molybdenum bronze (H_xMoO_3),[47] with a decrease and long-term retention of the cell resistance. This process corresponds to the LTP behavior of synapses. The reversibility of reactions (eqn (3)–(7)) upon changing the electric field polarity enables the reversible modulation of the SSE cell resistance, *i.e.*, the synaptic plasticity.

Similar EPSC behavior has also been observed in some proton-related lateral synaptic transistors.[48–51] If the aforementioned EPSC behavior arises from proton diffusion, the relaxation process will be affected by the temperature. Fig. 5(b) shows the EPSC measured at different temperatures from 293 to 353 K and their fitting by the stretched exponential function (eqn (1)). From the point of view of ion migration, the stretched exponential function could be used to describe a disordered system with a wide distribution of activation energies for ion conduction and an associated wide range of relaxation times among different relaxation processes,[52–54] which is consistent with the diffusion process of the randomly generated protons in the polycrystalline MoO_x films. In this case, the fitting values of τ could be used to describe the diffusion time of proton to reach equilibrium. The decrease of τ with increasing temperature indicates that the proton diffusion is thermally activated, becoming faster at higher temperatures. The Arrhenius plot of τ yields an activation energy of $E = 0.3$ eV for proton diffusion (see the inset in Fig. 5b), which is lower than that reported in proton-conducting oxides (about 0.4–0.5 eV).[45,46] This might be due to the higher water uptake from the ambient air (relative humidity $\sim$45% in our case).

The *I–V* hysteresis under the voltage sweep (see Fig. 1b) could be attributed to the retention property of the $Mo^{5+}(O_2)(OH)$ phase generated by the electrochemical doping process, *i.e.* LTP behavior. As the proton diffusion becomes faster with increasing temperature, the time to equilibrate the accumulated protons becomes shorter. Therefore, under the same voltage sweep rate and range, the electrochemical doping process and then the STP-to-LTP transition will be retarded because the generated protons have enough time to be relaxed in the films. Fig. 5(c) shows the *I–V* characteristics under different temperatures. The *I–V* hysteresis is clearly suppressed with increasing temperature, indicating a worse maintenance of the synaptic weight at elevated temperatures. A higher sweep speed and/or larger sweep range will be required to obtain the *I–V* hysteresis.

In previous reports, the synaptic functions have been demonstrated in two-terminal SSE cells with the ECM or VCM mode switching by tuning the conductive filaments with smaller size than the cell.[21,23,25] In our studies, the implementation of synaptic plasticity was realized by the interfacial electrochemical reaction of the cells, where the conductive filaments were not involved during the resistance switching and the abrupt change in cell resistance was successfully suppressed. Many intermediate resistance states can be obtained by simply varying identical pulse numbers. Such analog-type resistance switching behavior is useful for the adaptive learning operation of synaptic devices. Moreover, it should be pointed out that a certain extent of humidity is necessary for the synaptic behaviors of the

SSE cells.[28] Water molecules are, in a manner of speaking, ubiquitous in our living environment. The synapses within a living organism are also surrounded by a liquid environment. Taking the response to humidity and temperature into account, the SSE cells can be regarded as a smart artificial synapse with the potential to perceive the environment.

4. Conclusions

In summary, this study demonstrated that essential synaptic functions including potentiation and depression of synaptic weight, STP-to-LTP transition, STRP, and STDP behavior can be implemented in an Ag/MoO$_x$/FTO cell with analog-type resistance switching. The synaptic plasticity underlying these functions can be controlled by tuning the EPSC decay, which is determined by the applied voltage pulse number, width, frequency, and intervals between the pre- and post-spikes. The STP can be ascribed to the proton diffusion induced due to the concentration-gradient potential and the LTP can be ascribed to energetically stable phase (H$_x$MoO$_3$) generation induced by the electrochemical doping effect. These results indicate the possibility of achieving smart artificial synapse elements with SSE cells and will contribute to the development of artificial smart-terminal networking systems.

Acknowledgements

This work was supported by the National Natural Science Foundation of China (Grant No. 11274363, 11534015) and the Chinese Academy of Sciences (Grant No. XDB07030200, KJZD-EW-M05). D. S. acknowledges the support from the Opening Project of State Key Laboratory of High Performance Ceramics and Superfine Microstructure (Grant No. SKL201505SIC).

Notes and references

1 D. Kuzum, S. Yu and H. P. Wong, *Nanotechnology*, 2013, **24**, 382001.
2 D. Drachman, *Neurology*, 2005, **64**, 2004–2005.
3 G. Bi and M. Poo, *J. Neurosci.*, 1988, **18**(24), 10464–10472.
4 D. S. Jeong, I. Kim, M. Ziegler and H. Kohlstedt, *RSC Adv.*, 2013, **3**, 3169–3183.
5 S. D. Ha and S. J. Ramanathan, *J. Appl. Phys.*, 2011, **110**, 071101.
6 R. Waser, R. Dittmann, G. Staikov and K. Szot, *Adv. Mater.*, 2009, **21**, 2632–2663.
7 L. Goux and I. Valov, *Phys. Status Solidi A*, 2016, **213**, 274.
8 D. S. Shang, J. Sun, B. Shen and M. Wuttig, *Chin. Phys. B*, 2013, **22**, 067202.
9 K. Terabe, T. Hasegawa, T. Nakayama and M. Aono, *Nature*, 2005, **433**, 47–50.
10 A. Nayak, T. Tsuruoka, K. Terabe, T. Hasegawa and M. Aono, *Nanotechnology*, 2011, **22**, 235201.
11 S. H. Jo and W. Lu, *Nano Lett.*, 2008, **8**, 392–397.
12 C. Schindler, S. C. P. Thermadam, R. Waser and M. N. Kozicki, *IEEE Trans. Electron Devices*, 2007, **54**, 2762–2768.
13 R. Soni, P. Meuffels, H. Kohlstedt, C. Kügeler and R. Waser, *Appl. Phys. Lett.*, 2009, **94**, 123503.
14 K. Szot, W. Speier, G. Bihlmayer and R. Waser, *Nat. Mater.*, 2006, **5**, 312–320.
15 D. H. Kwon, K. M. Kim, J. H. Jang, J. M. Jeon, M. H. Lee, G. H. Kim, X. S. Li, G. S. Park, B. Lee, S. Han, M. Kim and C. S. Hwang, *Nat. Nanotechnol.*, 2010, **5**, 148–156.
16 M. J. Lee, C. B. Lee, D. Lee, S. R. Lee, M. Chang, J. H. Hur, Y. B. Kim, C. J. Kim, D. H. Seo, S. Seo, U. I. Chung, I. K. Yoo and K. Kim, *Nat. Mater.*, 2011, **10**, 625–630.
17 D. S. Shang, P. Li, T. Wang, E. Carria, J. Sun, B. Shen, T. Taubner, I. Valov, R. Waser and M. Wuttig, *Nanoscale*, 2015, **7**, 6023–6030.
18 K. Seo, I. Kim, S. Jung, M. Park, S. Jo, J. Park, J. Shin, K. P. Biju, J. Kong and K. Lee, *Nanotechnology*, 2011, **22**, 254023.
19 S. H. Jo, T. Chang, I. Ebong, B. B. Bhadviya, P. Mazumder and W. Lu, *Nano Lett.*, 2010, **10**, 1297–1301.
20 T. Ohno, T. Hasegawa, T. Tsuruoka, K. Terabe, J. K. Gimzewski and M. Aono, *Nat. Mater.*, 2011, **10**, 591–595.
21 T. Chang, S. H. Jo and W. Lu, *ACS Nano*, 2011, **5**, 7669–7676.
22 R. Yang, K. Terabe, Y. Yao, T. Tsuruoka, T. Hasegawa, J. K. Gimzewski and M. Aono, *Nanotechnology*, 2013, **24**, 384003.
23 Z. H. Tan, R. Yang, K. Terabe, X. B. Yin, X. D. Zhang and X. Guo, *Adv. Mater.*, 2015, **28**, 377–384.
24 S. Yu, B. Gao, Z. Fang, H. Yu, J. Kang and H.-S. P. Wong, *Adv. Mater.*, 2013, **25**, 1774–1779.
25 Y. Jeong, S. Kim and W. D. Lu, *Appl. Phys. Lett.*, 2015, **107**, 173105.
26 S. Kim, S. Choi, J. Lee and W. D. Lu, *ACS Nano*, 2014, **8**, 10262–10269.
27 Y. F. Wang, Y. C. Lin, I. T. Wang, T. P. Lin and T. H. Hou, *Sci. Rep.*, 2015, **5**, 10150.
28 C. S. Yang, D. S. Shang, Y. S. Chai, L. Q. Yan, B. G. Shen and Y. Sun, *Phys. Chem. Chem. Phys.*, 2016, **18**, 12466–12475.
29 T. V. P. Bliss and G. L. Collingridge, *Nature*, 1993, **361**, 31.
30 S. J. Martin, P. D. Grimwood and R. G. M. Morris, *Annu. Rev. Neurosci.*, 2000, **23**, 649.
31 D. C. Rubin and A. E. Wenzel, *Psychol. Rev.*, 1996, **103**, 734–760.
32 P. J. Sjöström, G. G. Turrigiano and S. B. Nelson, *Neuron*, 2001, **32**, 1149–1164.
33 F. Alibart, S. Pleutin, D. Guerin, C. Novembre, S. Lenfant, K. Lmimouni, C. Gamrat and D. Vuillaume, *Adv. Funct. Mater.*, 2010, **20**, 330–337.
34 Y. Li, Y. P. Zhong, J. J. Zhang, L. Xu, Q. Wang, H. J. Sun, H. Tong, X. M. Cheng and X. S. Miao, *Sci. Rep.*, 2014, **4**, 4906.
35 N. Caporale and Y. Dan, *Annu. Rev. Neurosci.*, 2008, **31**, 25–36.
36 L. F. Abbott and S. B. Nelson, *Nat. Neurosci.*, 2000, **3**, 1178–1183.
37 Y. Li, Y. Zhong, L. Xu, J. Zhang, X. Xu, H. Sun and X. Miao, *Sci. Rep.*, 2013, **3**, 1619.
38 C. Du, W. Ma, T. Chang, P. Sheridan and W. D. Lu, *Adv. Funct. Mater.*, 2015, **25**, 4290–4299.
39 M. Graupner and N. Brunel, *Proc. Natl. Acad. Sci. U. S. A.*, 2012, **109**, 3991.

40 T. Ronald, *Memristors and Memristive Systems*, Springer, New York, 2014.

41 R. C. Froemke and Y. Dan, *Nature*, 2002, **416**, 433–438.

42 T. Tappertzhofen, I. Valov, T. Tsuruoka, T. Hasegawa, R. Waser and M. Aono, *ACS Nano*, 2013, **7**, 6369.

43 I. Valov, E. Linn, S. Tappertzhofen, S. Schmelzer, J. Van den Hurk, F. Lentz and R. Waser, *Nat. Commun.*, 2013, **4**, 1771.

44 F. Messerschmitt, M. Kubicek and J. L. M. Rupp, *Adv. Funct. Mater.*, 2015, **25**, 5117.

45 E. Fabbri, D. Pergolesi and E. Traversa, *Chem. Soc. Rev.*, 2010, **39**, 4355.

46 K. D. Kreuer, *Annu. Rev. Mater. Res.*, 2003, **33**, 333–359.

47 J. J. Birtill and P. G. Dickens, *J. Solid State Chem.*, 1979, **29**, 367–372.

48 C. J. Wan, L. Q. Zhu, J. M. Zhou, Y. Shi and Q. Wan, *Nanoscale*, 2014, **6**, 4491.

49 L. Q. Zhu, C. J. Wan, L. Q. Guo, Y. Shi and Q. Wan, *Nat. Commun.*, 2014, **5**, 3158.

50 Y. H. Liu, L. Q. Zhu, P. Feng, Y. Shi and Q. Wan, *Adv. Mater.*, 2015, **27**, 5599.

51 C. J. Wan, L. Q. Zhu, Y. H. Liu, P. Feng, Z. P. Liu, H. L. Cao, P. Xiao, Y. Shi and Q. Wan, *Adv. Mater.*, 2016, **28**, 3557–3563.

52 K. L. Ngai, G. N. Greaves and C. T. Moynihan, *Phys. Rev. Lett.*, 1998, **80**, 1018.

53 K. L. Ngai and S. W. Martin, *Phys. Rev. B: Condens. Matter Mater. Phys.*, 1989, **40**, 10550.

54 J. Kakalios, R. A. Street and W. B. Jackson, *Phys. Rev. Lett.*, 1987, **59**, 1037.